



Characterization of the NEXT Hollow Cathode Inserts After Long-Duration Testing

*Jonathan A. Mackey, Rohit Shastry, and George C. Soulas
Glenn Research Center, Cleveland, Ohio*

NASA STI Program . . . in Profile

Since its founding, NASA has been dedicated to the advancement of aeronautics and space science. The NASA Scientific and Technical Information (STI) Program plays a key part in helping NASA maintain this important role.

The NASA STI Program operates under the auspices of the Agency Chief Information Officer. It collects, organizes, provides for archiving, and disseminates NASA's STI. The NASA STI Program provides access to the NASA Technical Report Server—Registered (NTRS Reg) and NASA Technical Report Server—Public (NTRS) thus providing one of the largest collections of aeronautical and space science STI in the world. Results are published in both non-NASA channels and by NASA in the NASA STI Report Series, which includes the following report types:

- **TECHNICAL PUBLICATION.** Reports of completed research or a major significant phase of research that present the results of NASA programs and include extensive data or theoretical analysis. Includes compilations of significant scientific and technical data and information deemed to be of continuing reference value. NASA counter-part of peer-reviewed formal professional papers, but has less stringent limitations on manuscript length and extent of graphic presentations.
- **TECHNICAL MEMORANDUM.** Scientific and technical findings that are preliminary or of specialized interest, e.g., “quick-release” reports, working papers, and bibliographies that contain minimal annotation. Does not contain extensive analysis.
- **CONTRACTOR REPORT.** Scientific and technical findings by NASA-sponsored contractors and grantees.
- **CONFERENCE PUBLICATION.** Collected papers from scientific and technical conferences, symposia, seminars, or other meetings sponsored or co-sponsored by NASA.
- **SPECIAL PUBLICATION.** Scientific, technical, or historical information from NASA programs, projects, and missions, often concerned with subjects having substantial public interest.
- **TECHNICAL TRANSLATION.** English-language translations of foreign scientific and technical material pertinent to NASA's mission.

For more information about the NASA STI program, see the following:

- Access the NASA STI program home page at <http://www.sti.nasa.gov>
- E-mail your question to help@sti.nasa.gov
- Fax your question to the NASA STI Information Desk at 757-864-6500
- Telephone the NASA STI Information Desk at 757-864-9658
- Write to:
NASA STI Program
Mail Stop 148
NASA Langley Research Center
Hampton, VA 23681-2199



Characterization of the NEXT Hollow Cathode Inserts After Long-Duration Testing

*Jonathan A. Mackey, Rohit Shastry, and George C. Soulas
Glenn Research Center, Cleveland, Ohio*

Prepared for the
35th International Electric Propulsion Conference
sponsored by IEPC
Atlanta, Georgia, October 8–12, 2017

National Aeronautics and
Space Administration

Glenn Research Center
Cleveland, Ohio 44135

Acknowledgments

The authors would like to thank Tim Sarver-Verhey, Mike Patterson, and John Yim for helpful comments and review of the work. Additional thanks is given to Kevin McCormick, Joy Buehler, Rick Rogers, Pete Bonacuse, and Terry McCue for their technical assistance with sample preparation and evaluation. This work was funded by the NEXT-C project, which is led by NASA Glenn Research Center under NASA's Science Mission Directorate.

Trade names and trademarks are used in this report for identification only. Their usage does not constitute an official endorsement, either expressed or implied, by the National Aeronautics and Space Administration.

Level of Review: This material has been technically reviewed by technical management.

Available from

NASA STI Program
Mail Stop 148
NASA Langley Research Center
Hampton, VA 23681-2199

National Technical Information Service
5285 Port Royal Road
Springfield, VA 22161
703-605-6000

This report is available in electronic form at <http://www.sti.nasa.gov/> and <http://ntrs.nasa.gov/>

Characterization of the NEXT Hollow Cathode Inserts After Long-Duration Testing

Jonathan A. Mackey, Rohit Shastry, and George C. Soulas
National Aeronautics and Space Administration
Glenn Research Center
Cleveland, Ohio 44135

Abstract

Hollow dispenser cathode inserts are a critical element of electric propulsion systems, and should therefore be well understood during long term operation to ensure reliable system performance. This work destructively investigated cathode inserts from the NEXT long-duration test which demonstrated 51,184 h of high-voltage operation, 918 kg of propellant throughput, and 35.5 MN-s of total impulse. The characterization methods used include scanning electron microscopy with energy dispersive spectroscopy and X-ray diffraction. Microscopy analysis has been performed on fractured surfaces, emission surfaces, and metallographically polished cross-sections of post-test inserts and unused inserts. Impregnate distribution, etch region thickness, impregnate chemical content, emission surface topography, and emission surface phase identification are the primary factors investigated.

Nomenclature

BSE	Backscattered Electron
DCA	Discharge Cathode Assembly
EDS	Energy Dispersive X-ray Spectroscopy
GRC	Glenn Research Center
IPS	Ion Propulsion System
LDT	Long-Duration Test
NCA	Neutralizer Cathode Assembly
NEXT	NASA's Evolutionary Xenon Thruster
NEXT-C	NASA's Evolutionary Xenon Thruster - Commercial
NSTAR	NASA's Solar Electric Propulsion Technology Application Readiness
PPU	Power Processing Unit
QCM	Quartz Crystal Microbalance
SE	Secondary Electron
SEM	Secondary Electron Microscope
XRD	X-ray Diffraction
ZAF	Mass, Absorption, Fluorescence Correction

1.0 Introduction

NASA has identified the need for a higher-power, higher-specific impulse, higher-thrust, and higher-throughput capable ion propulsion system (IPS) beyond the state-of-the-art NASA Solar Electric Propulsion Technology Application Readiness (NSTAR) IPS employed on the Deep Space 1 and Dawn Missions (Refs. 1 to 4). To fill this need, the NASA's Evolutionary Xenon Thruster (NEXT) IPS development, led by the NASA Glenn Research Center (GRC), was competitively selected in 2002.

The NEXT IPS advanced technology was developed under the sponsorship of NASA's In-Space Propulsion Technology Program, with Phase 2 close-out of the NEXT IPS development occurring in 2012. The highest fidelity NEXT hardware planned was built by the government/industry NEXT team and includes: an engineering model (referred to as prototype model) thruster, an engineering model power processor unit (PPU), engineering model propellant management assemblies, a prototype gimbal, and control unit simulators (Ref. 5). Each of the units underwent extensive component-level testing, completed environmental testing (with the exception of the PPU), and was tested together in system integration testing (Refs. 6 to 9). Results from IPS component testing and integration testing can be found in References 7 to 17.

The NEXT thruster service life capability is being assessed through a comprehensive service life validation scheme that utilizes a combination of testing and analyses. Since the NEXT thruster is an evolution of the NSTAR thruster design, insights into the operation and erosion processes gained from NSTAR's development project apply to the NEXT thruster. The NEXT thruster, as a second-generation deep-space gridded ion thruster, made use of over 70,000 h of ground and flight test experience (not including the accumulated hours from the NSTAR IPS on the ongoing Dawn mission) in both the design of the NEXT thruster and evaluation of thruster wear-out failure modes. A NEXT service life assessment was conducted at NASA GRC, employing several models to evaluate all known failure modes with high confidence based upon the substantial amount of ion thruster testing dating back to the early 1960s (Refs. 18 and 19). The NEXT service life assessment also incorporated results from the NEXT 2,000 h wear test conducted on a NEXT laboratory model (referred to as engineering model) thruster operating at full power (6.9 kW) (Refs. 18 and 20). The transparency between the engineering model and prototype model thruster wear characteristics was demonstrated by a short-duration prototype model wear test (Ref. 21). The references for the NEXT service life assessment explain the thruster performance and erosion modeling analyses (Refs. 18 and 19).

The NEXT Long-Duration Test (LDT) was initiated in June 2005 as part of the comprehensive thruster service life assessment. The goals of the test were to demonstrate the initial project qualification propellant throughput requirement of 450 kg, validate the thruster service life model's predictions, quantify thruster performance and erosion as a function of thruster wear and throttle level, and identify any unknown life-limiting mechanisms. In December 2009, after successfully demonstrating the original qualification throughput requirement of 450 kg, the first listed goal was redefined to test to failure of the thruster or until decision to terminate the test voluntarily.

A decision to voluntarily terminate the test was made in April 2013 due to budget constraints. After a comprehensive end-of-test performance characterization was completed (Ref. 22), the thruster was vented to atmospheric conditions in April 2014. At the end of the test, the thruster had accumulated 51,184 h of high-voltage operation, processed 918 kg of xenon propellant, and delivered 35.5 MN-s of total impulse, setting numerous records for the most demonstrated lifetime of an electric propulsion device. Post-test inspection of the hardware was initiated soon after removal of the thruster from the vacuum facility. The results of this inspection for the discharge and neutralizer cathode inserts are the topic of this paper. Results for other thruster components, including the ion optics, discharge chamber, and cathode assemblies, are covered in companion publications (Refs. 23 and 25).

In April 2015, Aerojet Rocketdyne (with subcontractor ZIN Technologies) was competitively selected for the NASA's Evolutionary Xenon Thruster – Commercial (NEXT-C) contract. The objectives of this contract are two-fold: (1) To deliver two flight thrusters and two PPUs for use in future NASA missions, and (2) take steps to transition NEXT into a commercially available, off-the-shelf IPS for use by NASA as well as commercial spacecraft providers. While the LDT was initiated as part of the Phase 2 effort under NASA's In-Space Propulsion Technology Program, the post-test inspection of the LDT thruster hardware has now fallen under the NEXT-C project to be performed as an in-house task by GRC. The results of the LDT will then be relayed to Aerojet Rocketdyne along with any recommended design improvements to be made to the thruster flight design.

The paper is organized as follows: Section 2.0 covers the background for the NEXT LDT, including details of the test article as well as the throttling profile used over the course of the test. Section 3.0 describes the post-test inspection objectives, as well as the overall approach that was taken. Section 4.0 includes major results of the post-test inspection for the cathode inserts. Section 5.0 then summarizes key findings.

2.0 NEXT Long-Duration Test Background

The NEXT LDT was conducted within Vacuum Facility 16 at NASA GRC. The test article is a modified version of an engineering model (designated EM3), shown firing in Figure 1. To obtain a flight-representative configuration, prototype-model ion optics were incorporated, provided by industry partner Aerojet Corporation (now Aerojet Rocketdyne). A graphite discharge cathode keeper electrode was also incorporated into EM3 (Ref. 26). The NEXT thruster is nominally a 0.5 to 6.9 kW input power xenon thruster utilizing 2-grid dished-out ion optics, capable of producing thrust levels of 25 to 235 mN and specific impulses of 1400 to 4160 s. The technical approach for NEXT continues the derating philosophy used for the NSTAR ion thruster. A beam extraction area of 1.6X that of NSTAR allows for higher thruster input power while maintaining low discharge voltages and ion current densities, thus maintaining thruster longevity. Additional descriptions of the hardware, including the NEXT EM3 design and vacuum facility, can be found in References 2, 27, and 28 to 32. Various diagnostics were used to characterize the performance and wear of the thruster during the LDT, details of the testing and facility diagnostics can be found in References 30 and 33.

The NEXT IPS was designed for solar electric propulsion applications that experience variable input power as the available solar flux changes with distance from the Sun throughout the mission. For the LDT, the EM3 thruster was operated in a mission-representative profile comprised of discrete segments at various power levels shown in Table 1 and described in detail in Reference 34. The thruster was operated at each of these segments for sufficient duration to characterize the performance and wear rates, and to validate the thruster service life models. The throttle profile was completed in May 2010 and the thruster was then operated at full power until the end of the test in February 2014. For the majority of the test, detailed performance characterizations were carried out at 11 of the 40 operating conditions in the NEXT throttle table. These characterizations included overall thruster performance as well as component performance of the discharge chamber, neutralizer cathode, and ion optics. A comprehensive performance characterization was also performed at the end of the test that included all 40 operating conditions in the NEXT throttle table. Details of performance measurements as well as in situ images taken during the test can be found in References 22, 29, 30, and 33 to 41.

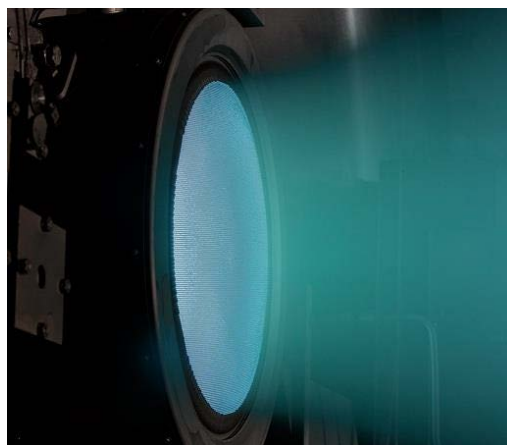


Figure 1.—Photograph of NEXT EM3 firing within vacuum facility 16 at GRC.

TABLE 1.—NEXT LONG-DURATION TEST MISSION-REPRESENTATIVE THROTTLING PROFILE

Throttle segment	Throttle level	Input power, kW	Operating condition	Segment duration, kh	End of segment date
1	TL40	6.9	3.52 A, 1800 V	13.0	11/17/2007
2	TL37	4.7	3.52 A, 1179 V	6.5	12/23/2008
3	TL05	1.1	1.20 A, 679 V	3.4	06/24/2009
4	TL01	0.5	1.00 A, 275 V	3.2	12/15/2009
5	TL12	2.4	1.20 A, 1800 V	3.1	05/05/2010
6	TL40	6.9	3.52 A, 1800 V	21.9	02/28/2014

3.0 Post-Test Inspection Objective and Approach

The post-test inspection for the NEXT LDT largely followed the same approach and processes employed for the inspection of the NSTAR Extended Life Test thruster hardware (Ref. 42). The primary objectives of the post-test inspection are: measure critical thruster wear rates that can induce thruster failure to verify both in situ measurements and the service life model predictions; resolve any thruster-related issues encountered during the NEXT LDT; verify that thruster design changes made as a result of prior wear test findings had the desired impacts; and identify any unanticipated life-limiting phenomena. The thruster components were first inspected non-destructively in order to preserve the hardware for potential future testing. It was originally thought that resolution of issues encountered during the test or further characterization of the state of the hardware may require additional operation of individual components or the thruster as a whole. However, after reviewing results from the non-destructive inspection, it was determined that resolution of many open issues and questions required destructive inspection of various thruster components.

Particular attention was paid to failure modes that were identified during the initial lifetime assessment and service life modeling for the NEXT thruster (Ref. 18). For the cathodes, these failure modes included: insert barium depletion resulting in excessive cathode temperatures or inability to ignite; excessive wear of the keeper orifice plate (discharge cathode) or keeper tube (neutralizer cathode) resulting in exposure of the cathode orifice plate and heater; excessive wear of the cathode orifice plate; heater mechanical failure from cyclic operation; and neutralizer cathode orifice clogging preventing proper cathode operation. The cathode inserts are the focus of this work, a companion paper has discussed the results of the remaining cathode components (Ref. 23).

At the conclusion of the LDT the cathode inserts were ignited using a slow ramping DC voltage rather than the typical pulsing ignition, this was done to operationally characterize insert health. Two ignition attempts were successfully completed on both cathode inserts, at relatively low starting voltages. This successful set of low voltage ignition attempts indicated no severe insert degradation. The remainder of this work describes the destructive analysis performed to characterize the post-test condition of the inserts.

The neutralizer cathode assembly (NCA) and discharge cathode assembly (DCA) hollow tube inserts have been investigated using scanning electron microscopy (SEM) at 15 kV and 15 μ A with energy dispersive spectroscopy (EDS) with a standard-less EDAX system, and x-ray diffraction (XRD). In order to establish a baseline, each measurement was made on both the inserts used during the LDT and unused inserts from the same batch. The unused inserts were kept sealed in their original packaging and were stored during the duration of the LDT. As much as possible the two sets of inserts, hereafter referred to as the “LDT” and “unused” inserts, were prepared and handled in the same fashion and in similar time periods. As a result, the study investigated a total of four hollow tube inserts (1) unused NCA, (2) LDT NCA, (3) unused DCA, and (4) LDT DCA. Each insert was cross-sectioned length-wise on a diamond blade without cutting fluid, to avoid contaminating the samples. One half of each sample was mounted in epoxy and metallographically polished, the remaining half was left un-mounted for examination of the inner emission surface.

The mounted halves were polished to the extent possible in accordance with the work of Kan and Seaver (Ref. 42). Silicon carbide polishing paper was used with kerosene as a working fluid, to minimize moisture exposure of the inserts. Samples were hand polished with medium pressure for roughly 1 min at each grit of polishing paper from –250, –400, –600, –800, to –1200. Finally, samples were hand polished on a Struers DAC-MD cloth for 2 min with only kerosene as the working fluid. Samples were cleaned with lens paper and kerosene between each step of polishing, no sonication cleaning was used. Material loss was tracked using calipers during the polishing process. On average the polishing process removed 0.2 mm of material, with the majority of losses occurring during the –250 and –400 grit silicon carbide steps. Polished samples were carbon coated for effective SEM/EDS characterization. Carbon coating was performed to ensure a thin ideally uniform coating of carbon using a short duration (roughly 2 s) carbon sputtering process. Polished/coated samples were evaluated in SEM/EDS along the cross-sectioned region of the hollow tube inserts. Given cutting uncertainty and the polishing process the cross-section is estimated to be within 0.9 mm of insert centerline.

The un-mounted halves were preserved for evaluation of the inner emission surface. The topography of the inner emission surface was evaluated by examining the surface with SEM, with a sample tilt angle of 45° to reveal surface features. Both secondary electron (SE) and backscattered-electron (BSE) detectors were used to highlight topographical features and chemical contrast, respectively. The un-mounted halves were also evaluated using XRD to determine crystalline phases on the inner emission surfaces. The XRD system was setup with 45 kV 20 mA cobalt radiation in a Bragg-Brentano configuration, using parallel beam optics to collect on the curved inner surface. Samples were mounted such that the beam oriented along the axial direction of the samples. Data was collected from 25 to 100° 2-theta, over the course of 2 h. Spot size was controlled to match the width of the insert and an axial length of 4.5 mm at 100° 2-theta and 20.1 mm at 25° 2-theta.

Samples were evaluated in at least three axial locations. The axial locations were determined by their axial distance from the downstream inner radius corner serving as the origin. The “downstream” location was 0.5 mm from the origin, the “central” location was within 3 mm of the midpoint, and the “upstream” location was within 3 mm of the upstream first quarter-point. For several measurements, a volumetric weighted average across the three axial locations has been calculated for simple insert to insert comparison. In general, the deviation between the axial locations was used as an estimation on the weighted average uncertainty, although generally the total uncertainty is likely to be larger.

4.0 Results and Discussion

4.1 Impregnate Size, Distribution, and Area Fraction

Image processing on BSE micrographs provided a mechanism to quantitatively measure impregnate grain size, distribution, and area fraction. The chemical contrast of BSE images allowed for extraction of the impregnate grains using Huang-Wang image thresholding method. Typical BSE micrographs and analyzed images are shown in Figure 2, showing the unused NCA and DCA inserts at the central axial location. Impregnate grains were measured for circularity ‘C’, defined as a ratio of the grain cross-sectional area ‘A’ and perimeter ‘P’ ($C = 4\pi A/P^2$). The impregnate grains have a wide range of circularity with mean values between 0.4 and 0.5 indicating grains are generally elongated regions with some thin features. In cross-section the grains have some visible local connectivity, but no observable global connectivity. A full 3D rendering of the microstructure would expectedly reveal a fully connected network of impregnate grains, but constructing a 3D model was beyond the scope of this work.

The impregnate phase area fraction of the micrographs provides a means of roughly quantifying the volume fraction of the impregnate phase, which is proportional to the tungsten matrix porosity. The results of the inserts are summarized in Table 2, where each insert has been evaluated at the upstream/central/downstream axial locations along the mid radius of the cross-section, and a weighted average estimate of the whole insert. No clear trends in axial location exist, so the insert weighted average value can be used for insert to insert comparison. The unused and LDT inserts have the same nominal

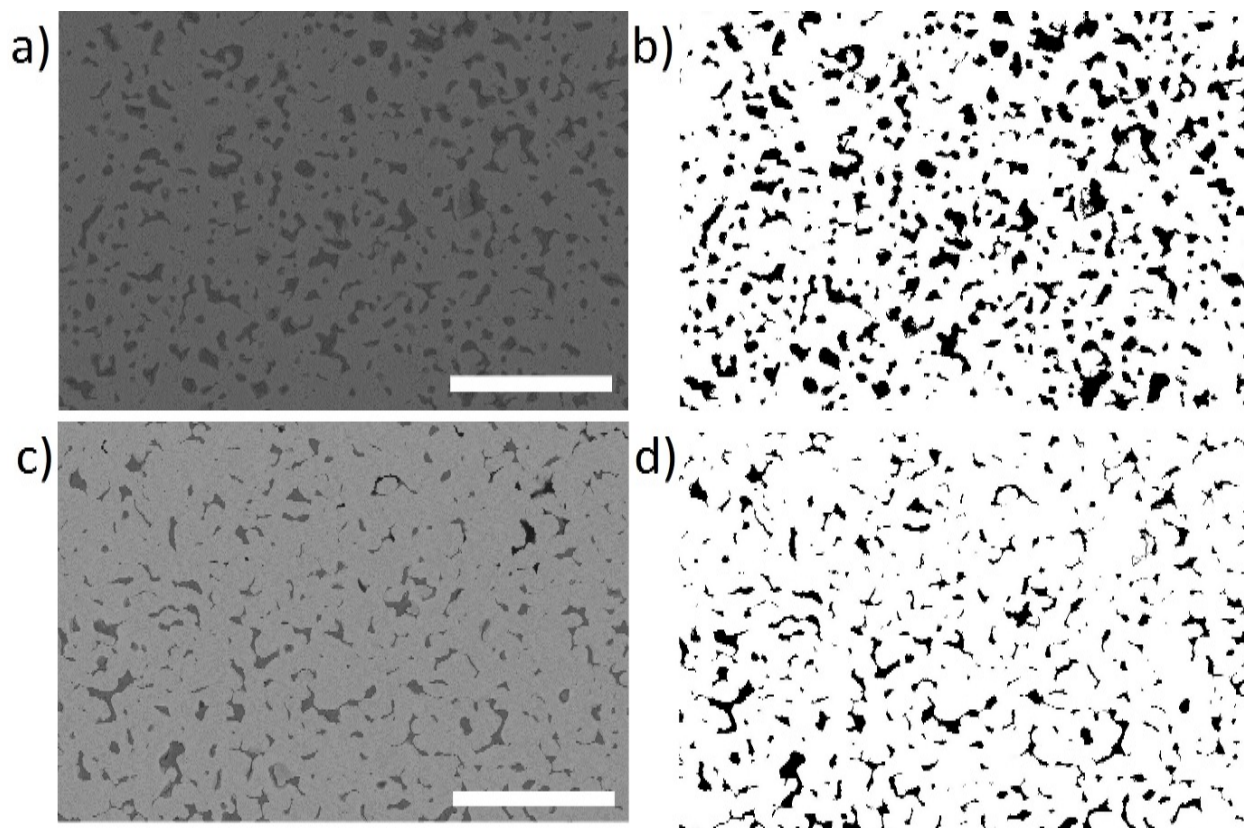


Figure 2.—Unused inserts (a) BSE micrograph of NCA insert (scale bar 50 μm), (b) calculated impregnate grain masks of NCA BSE micrograph, (c) BSE micrograph of DCA insert (scale bar 50 μm), (d) calculated impregnate grain masks of DCA BSE micrograph.

TABLE 2.—IMPREGNATE AREA FRACTION

Insert	Upstream, area percent	Central, area percent	Downstream, area percent	Weighted average, area percent
Unused NCA	17.1	17.5	17.2	17.2 \pm 0.4
LDT NCA	17.4	20.0	17.2	18.4 \pm 3.0
Unused DCA	10.7	9.0	12.6	10.4 \pm 3.6
LDT DCA	10.4	10.0	10.3	10.2 \pm 0.4

weighted average impregnate area percent within uncertainty, indicating no significant microstructural changes to the tungsten matrix and impregnate phase during the LDT. A clear difference between the NCA and DCA impregnate area fraction exists and is being further investigated. It is suspected that the difference is due to the geometric differences between the two inserts, but it is not known if the difference is a measurement artifact or indicates an actual difference between the inserts. The lower area fraction of the DCA insert can be visually observed in Figure 2(d) compared to the NCA insert in Figure 2(b). The weight gain during impregnation of both the NCA and DCA inserts was within specification, therefore the measured area fraction difference is not believed to be a significant concern.

The size distribution of impregnate grains is shown in Figure 3 for all four inserts. The histograms represent a weighted average dataset based on image analysis of grain size at upstream/central/downstream locations. The image analysis consisted of (1) calculating a ferret/caliper diameter across >500 impregnate grains which were greater than 0.1 μm , and (2) generating a count frequency based histogram, then (3) using the average histogram bin diameter to estimate the area frequency based histogram assuming circular grains. The count based analysis, Figure 3(a), shows the majority of grains to be smaller than 2 μm with a monotonic decrease for larger sized grains. The count based histograms are

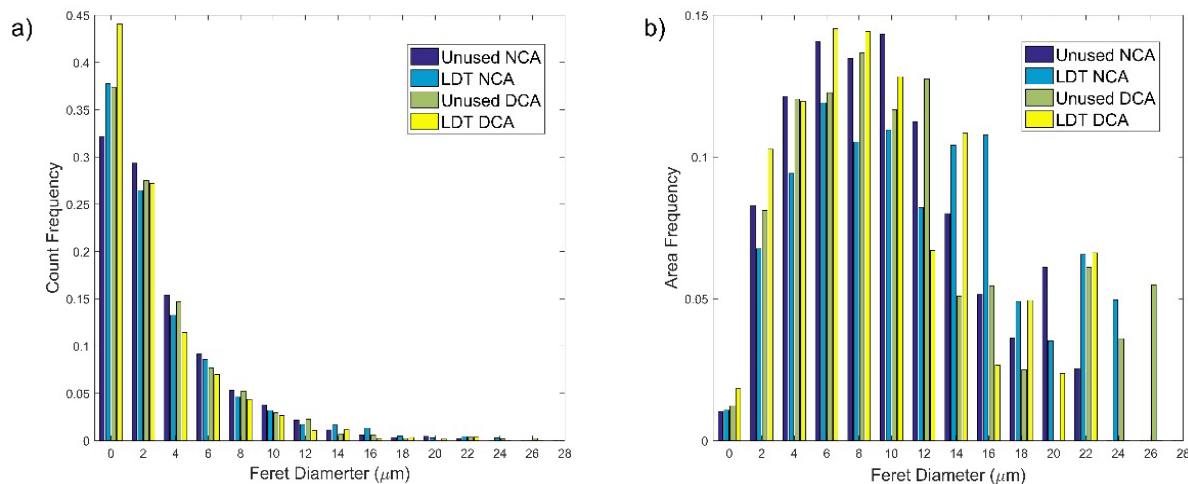


Figure 3.—Impregnate grain size histograms (a) count frequency and (b) area frequency, averaged across upstream/central/downstream axial locations from each insert.

more sensitive to micrograph resolution and image analysis settings, as very small regions can easily be misidentified as individual impregnate phases. A more reliable metric is to calculate an area frequency from the approximate grain size. In this method, the quantity of impregnate material in each grain is better represented and negligibly small regions are less significant. Figure 3(b) shows the area frequency of all four inserts, indicating the majority of impregnate material is contained in grains between 4 and 12 μm . The chemical analysis to follow was performed preferentially on impregnate grains in the 4 and 12 μm range, to gain a representative indication of the majority of the impregnate. The trends of impregnate grain size between all four inserts are qualitatively and quantitatively similar, indicating that no significant microstructural modifications of the impregnate grains have occurred during the LDT or between the NCA and DCA inserts.

4.2 Impregnate Etched Regions

During processing of the inserts, an etching step is used to remove impregnate from the surface of the inserts. During operation it is possible for impregnate to transport within this region, therefore it is desirable to quantify this etched region. The etched regions on the inserts were measured from back-scattered electron micrographs to reveal the contrast difference between pores filled with impregnate material and pores filled with epoxy potting compound. Figure 4 is a typical micrograph of an etch region, shown is the unused NCA insert inner etch region at the central axial location. Pores filled with epoxy potting compound show as black, while impregnate filled pores show as dark gray, the tungsten matrix is the remaining light gray phase. The blue line indicates the inner edge of the tungsten matrix and the green line indicates the inner edge of the impregnate region. The distance between the blue and green lines is measured as the etch region thickness in Table 3, a similar approach was used at the outer edges. The placement of the blue and green lines is somewhat arbitrary and introduces a fair amount of uncertainty to the measurement, as a result the thickness measurements are averages along 120 μm axial distances with $\pm 5 \mu\text{m}$ uncertainty in the thickness. Etch thickness measurements have been made at both the inner and outer surfaces and at the upstream/central/downstream locations on all four inserts. In general the thickness of the etch region decreased as a result of the LDT testing, but the measurement is inherently hindered by low sampling statistics and relatively large measurement uncertainty. On average the etch thickness decreased by 20 to 30 percent between the unused inserts and the LDT inserts across the central and downstream axial regions of the inserts. The decrease in etch region thickness may indicate impregnate transport within the insert open pore network toward the inner and outer surfaces.

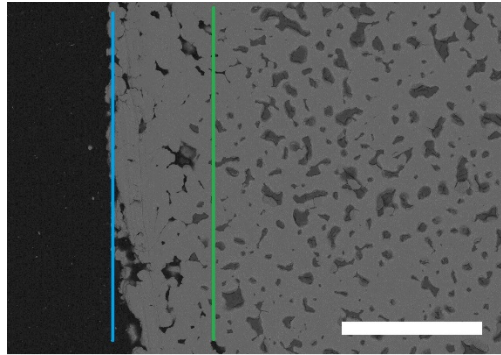


Figure 4.—Unused NCA inset showing inner etch region, at central axial location. Blue line indicates inner edge of tungsten matrix, green line indicates inner edge of impregnate. Scale bar 50 μm .

TABLE 3.—ETCH REGION THICKNESS

Insert	Upstream		Central		Downstream	
	Inner, μm	Outer, μm	Inner, μm	Outer, μm	Inner, μm	Outer, μm
Unused NCA	36.0 \pm 5.0	15.0 \pm 5.0	37.0 \pm 5.0	17.0 \pm 5.0	27.0 \pm 5.0	21.0 \pm 5.0
LDT NCA	15.0 \pm 5.0	34.0 \pm 5.0	25.0 \pm 5.0	0.0 \pm 5.0	23.0 \pm 5.0	10.0 \pm 5.0
Unused DCA	62.0 \pm 5.0	49.0 \pm 5.0	57.0 \pm 5.0	47.0 \pm 5.0	61.0 \pm 5.0	49.0 \pm 5.0
LDT DCA	39.0 \pm 5.0	52.0 \pm 5.0	40.0 \pm 5.0	40.0 \pm 5.0	59.0 \pm 5.0	36.0 \pm 5.0

Chemical potential gradients or thermal gradients may be the driving factors in the transport, but further investigation into the driving mechanisms was beyond the scope of this work. The upstream axial region outer radius indicates an alternative behavior, an increase in the etch thickness during operation. This increase in etch thickness may indicate impregnate transport away from the outer surface or impregnate removal from pores without subsequent replacement from impregnate bulk. Possibly this is some indication of bulk impregnation depletion, or simply a redistribution of impregnate due to a thermally driven condition. The upstream axial region is the coolest region during operation, so possibly the impregnate is driven toward the hotter sections. In any case the changes in etch region thickness do not clearly indicate any significant loss of impregnate or failure mechanisms.

4.3 Impregnate Chemical Analysis

The chemical variability of a single grain of impregnate is shown in Figure 5. Variation is expected to arise from a number of possible sources including measurement artifacts, such as EDS interaction volume size relative to impregnate grain size, and actual sample variation, arising from non-homogeneous distributions. Six locations evenly spaced across a typical sized impregnate grain were evaluated using the carbon $K\alpha$, oxygen $K\alpha$, aluminum $K\alpha$, calcium $K\alpha$, barium $L\alpha$, and tungsten $L\alpha$ line intensities. Intensity data has been normalized as counts per time over the course of 50 s of sampling. As expected the primary constituents are barium, oxygen, aluminum, and calcium. Carbon is a result of carbon coating the samples for electrical conductivity and tungsten is a result of EDS interaction volume being near the size of impregnate grains and therefore sampling some of the surrounding matrix. As a result, the tungsten intensity is highest at both the first and last locations evaluated. Across the six points, the variability of any single constituent can be large; using barium as the metric a standard deviation of 20 percent is established. EDS data is most reliable for qualitative comparison of line intensities such as Ba/Al content of the impregnate, but it can also be used to estimate semi-quantitative atomic percent. A standard-less ZAF correction method has been used (Z = atomic number, A = absorption, F = fluorescence) to estimate

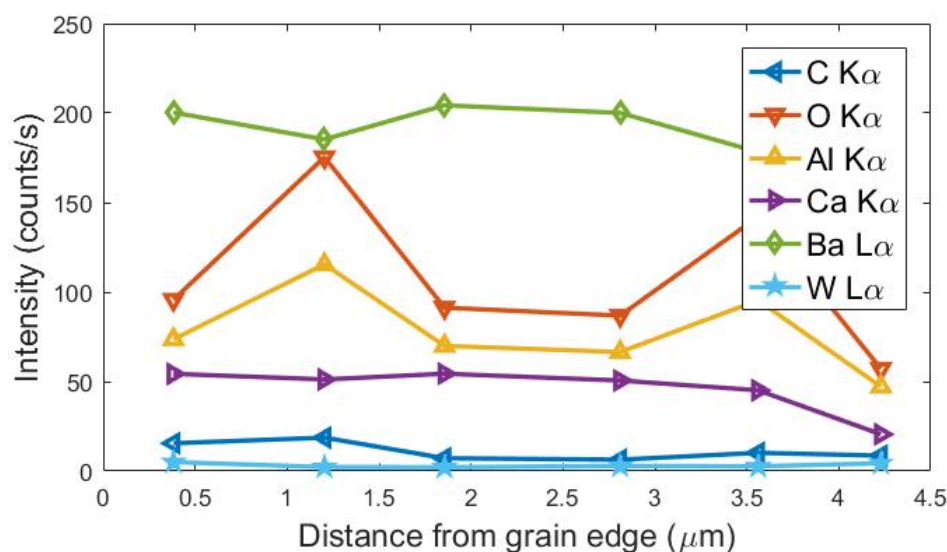


Figure 5.—Impregnate grain chemical variability as a function of location within a typical grain.

barium, aluminum, calcium, and tungsten atomic percent of impregnate grains. The barium, aluminum, and calcium atomic percent estimations have been used to calculate BaO, Al₂O₃, and CaO content of the impregnate phase.

Each of the four inserts has been evaluated across the full width of the cross-section in the radial direction at several typical sized impregnate grains (4 to 6 μm). EDS data was collected on each grain at 2,000 times magnification to ensure reliable beam placement near the grain centroid to reduce sampling of the matrix. Distances from the inner radius were tracked by aligning a series of lower magnification micrographs across the insert width. The measurements were repeated at the upstream/central/downstream axial locations. The collection of impregnate Ba/Al intensity data is shown in Figure 6 for all four inserts at three axial locations. The Ba/Al intensity ratio is indicative of the bulk barium content of the impregnate, aluminum was used as the normalizing factor because was not expected to migrate from the system as much as barium or calcium. Tungsten cannot be used as the normalizing factor because the volume of tungsten matrix sampled with each measurement can vary from impregnate grain to impregnate grain. Representative error bars based on the standard deviation of the single impregnate grain chemical variability are added to the LDT upstream dataset for reference. The NCA inserts exhibit little to no bulk difference in Ba/Al intensity between the unused and LDT inserts. The Ba/Al intensity has no clear trends in either radial or axial directions, rather grain to grain variability dominates the data. No regions of Ba depletion were identified throughout the NCA inserts, including near the emission region at the inner surface and downstream axial location. The unused NCA, LDT NCA, and unused DCA inserts all compare well in Ba/Al intensity in both mean value and scatter across the insert. However, the LDT DCA insert, shown by green symbols in Figure 6(b), indicate a generally lower Ba/Al intensity uniformly across the insert. This is possibly an indication of Ba loss from the insert during the LDT test. Additionally, small local regions of low Ba/Al content have been observed in the LDT DCA insert. No similar local region of low Ba/Al content was observed in the LDT NCA insert. Regions near the inner and outer downstream axial location indicate Ba/Al intensity ratios less than unity.

Figure 7 shows a typical Ba/Al intensity profile for the LDT DCA downstream insert near the inner emission surface. The profile was calculated from the inner emission surface in the radial direction and therefore partially overlaps with the etch region, shown to be 59 μm in Table 3. A clear jump in Ba/Al intensity is observed around 75 to 80 μm radially from the inner surface. For insert geometric radii smaller than 75 μm the Ba/Al intensity is around 0.6, for radii larger than 75 μm the intensity matches with the bulk Ba/Al intensity. Corresponding to the region of low Ba/Al intensity was a region of nearly no Ca/Al intensity, beyond 75 μm the intensity matches with the bulk Ca/Al intensity. A similar profile

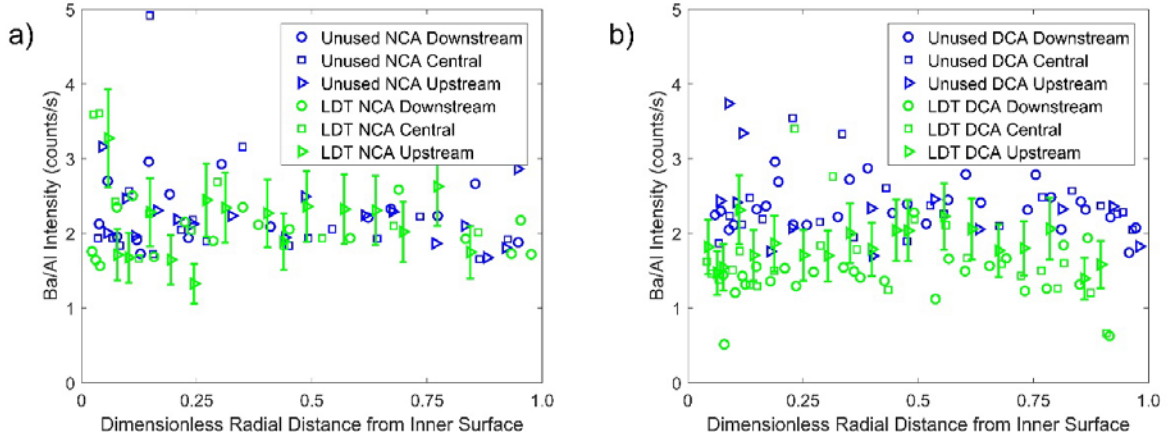


Figure 6.—Ba/Al intensity of impregnate grains at various axial locations for (a) unused and LDT NCA inserts and (b) unused and LDT DCA inserts.

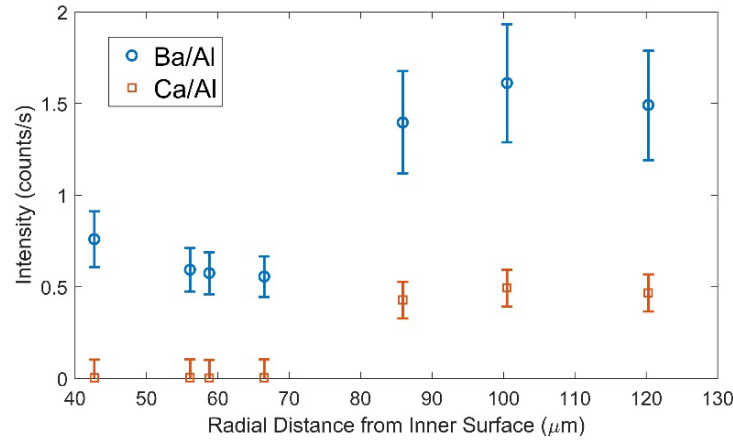


Figure 7.—Barium depletion depth indicated by Ba/Al intensity jump in LDT DCA downstream axial location.

has been observed throughout the downstream section of the LDT DCA insert at several axial locations measured at 0.5 mm intervals. In all cases the Ba/Al jump was found within 45 to 88 μm of the inner surface, in regions where the etch thickness was determined to be 34 to 84 μm . The uncertainty on both the jump location and the etch thickness was ± 5 μm . Similar barium depletion zones have been identified on the NSTAR discharge cathode assemblies after 30,472 h of operation (Refs. 44 and 45). The Ba/Al depletion depth is a possible predictor of insert lifetime, but the critical depth at which operation becomes limited is difficult to identify.

Using ZAF correction the $\text{BaO}/\text{Al}_2\text{O}_3$ content has been estimated across all inserts. The bulk data in Figure 6 was processed to determine $\text{BaO}/\text{Al}_2\text{O}_3$ content radially averaged across the inserts at the three axial locations, the data is presented in Table 4. The values indicate that the unused NCA, LDT NCA, and unused DCA inserts all have comparable levels of $\text{BaO}/\text{Al}_2\text{O}_3$ content and no general trends in the axial direction. The uncertainty for each value is a 95 percent confidence interval based on the scatter of the data across the radius of the inserts. The $\text{BaO}/\text{Al}_2\text{O}_3$ content estimated for the unused NCA, LDT NCA, and unused DCA inserts match well with the target nominal composition of the inserts. The LDT DCA insert, which showed a region of local barium depletion, also indicates a lower bulk $\text{BaO}/\text{Al}_2\text{O}_3$ content. An axial profile exists along the LDT DCA insert, with the most $\text{BaO}/\text{Al}_2\text{O}_3$ content remaining at the upstream end, and the lowest $\text{BaO}/\text{Al}_2\text{O}_3$ content at the downstream end where the depletion region was observed. The barium depleted region of the LDT DCA insert is a small region in comparison to the full insert width, so the data presented in Table 4 is an indication of bulk values and not simply a measure of the local depleted region.

TABLE 4.—IMPREGNATE BaO/Al₂O₃ CONTENT

Insert	Upstream (g-BaO/g-Al ₂ O ₃)	Central (g-BaO/g-Al ₂ O ₃)	Downstream (g-BaO/g-Al ₂ O ₃)	Weighted average (g-BaO/g-Al ₂ O ₃)
Unused NCA	9.3±1.9	9.1±1.5	9.7±1.2	9.3±1.4
LDT NCA	8.7±1.4	9.6±1.8	8.0±0.6	8.9±1.3
Unused DCA	9.5±1.4	9.6±0.9	9.4±0.5	9.5±1.4
LDT DCA	7.4±0.5	6.6±0.9	5.7±0.6	6.7±1.0

TABLE 5.—INNER SURFACE PHASE IDENTIFICATION

Insert	Upstream	Central	Downstream
Unused NCA	N/A	W	N/A
LDT NCA	W, Ba ₃ W ₂ O ₉ , Ba ₂ WO ₅ , Ba ₃ WO ₆ , BaWO ₄	W, Ba ₄ Al ₂ O ₇ , Ba ₃ WO ₆ , Ba ₃ Al ₂ O ₆	BaCa(CO ₃) ₂ , W
Unused DCA	N/A	W	N/A
LDT DCA	W, Ba ₂ CaWO ₆	W, Ba ₂ CaWO ₆	N/A

The insert weighted average BaO/Al₂O₃ content is another possible predictor of insert life. Like the depletion depth method, difficulties exist in determining the BaO/Al₂O₃ content below which operation becomes limited, determining the magnitude of this limit is beyond the scope of this work. As an example, the insert life can be predicted for arbitrarily assumed minimum BaO/Al₂O₃ limits. Using the data of Table 4 the NCA insert has a nominal decrease of 4 percent after 51,771 h of high-voltage operation, and the DCA has a nominal decrease of 30 percent after 51,724 h of high-voltage operation. Only the 30 percent decrease of the DCA insert is beyond the uncertainty of the measurement. Therefore, assuming reliable operation monotonically down to a BaO/Al₂O₃ loss of 75 percent, the predicted lifetime of the DCA insert is beyond 130,000 h, and the lifetime of the NCA cannot be determined.

4.4 Emission Surface Phase Identification

The un-mounted insert halves were preserved for examination of the inner emission surface. Phase identification of the inserts was achieved using XRD, employing parallel beam optics to collect diffraction data from the inside of a curved surface. Beam physical dimensions were controlled in an attempt to capture upstream, central, and downstream axial location data, but low angle diffraction data causes the incident beam to capture several axial regions within a single scan. The XRD scans were evaluated using Rietveld whole pattern fitting techniques to estimate quantitative values of the phases identified, but given the complexity of a varying beam length the quantitative data is only used to order the phases by content. Table 5 lists the phases observed across the four inserts. Phases are listed in order with the first phase being the main phase and the last phase being the smallest content detected, quantitative analysis was based on weight percent. The NCA and DCA unused inserts have clean inner surfaces composed of pure cubic W (space group:Im-3m (Ref. 46)), with no indication of impregnate, tungstates, or foreign contamination.

The LDT NCA insert visually has several banded regions of color contrast. The downstream region of the LDT NCA insert has a white appearance and is composed of monoclinic BaCa(CO₃)₂ (space group: P2₁/m (Ref. 47) with cubic W as the secondary phase. The carbon source to form the BaCa(CO₃)₂ phase is likely facility back-sputter, and therefore an artifact of ground testing and not representative of a flight cathode. The white band seems to align with the shadow region of the orifice plate, further supporting the theory that the carbon is a facility artifact. The central region of the LDT NCA insert is composed of bands of light gray, dark gray, and white. The observed phases include primarily cubic W with orthorhombic Ba₄Al₂O₇ (space group:Ccm (Ref. 48)), cubic Ba₃WO₆ (space group:Fm-3m (Ref. 49)), and cubic Ba₃Al₂O₆ (space group:Pa-3 (Ref. 50)) phases. The phases have not been identified to match the three color bands. The orthorhombic Ba₄Al₂O₇ and cubic Ba₃Al₂O₆ phases correspond to the 4:1 and 3:1 ratios of the BaO and Al₂O₃ oxides present in the impregnate. A solid solution of these 4:1 and 3:1 phases are stable between 940 and 1500 °C which covers the expected temperature range of the central portion of the NCA insert (Ref. 51). The cubic Ba₃WO₆ phase is stable between 805 and 1590 °C also covering the

expected operating range, below 805 °C the tetragonal phase is stable (Ref. 52). The tetragonal phase was not observed on the insert. The barium aluminate phases are possibly a reactant in the process to evolve gaseous barium from the impregnate, while the barium tungstate is likely a byproduct of the reaction (Refs. 52 and 53). The upstream section of the insert is primarily covered in a single large dark band. The observed phases include primarily cubic W with rhombohedral $\text{Ba}_3\text{W}_2\text{O}_9$ (space group:R-3c (Ref. 54)), orthorhombic Ba_2WO_5 (space group:Pnma (Ref. 55)), cubic Ba_3WO_6 (space group:Fm-3m (Ref. 49)), and tetragonal BaWO_4 (space group:I41/a (Ref. 56)). These tungstate phases correspond to the 3:2, 2:1, 3:1, and 1:1 ratios of the BaO and WO_3 oxides. The orthorhombic Ba_2WO_5 and tetragonal BaWO_4 phases are stable in solid solution between room temperature and 1320 °C (Ref. 52). The barium tungstate phases are likely a byproduct of the reaction to generate gaseous barium (Refs. 53 and 57). The BaWO_4 phase has been previously identified on a lifetime tested NASA cathode insert (Ref. 58).

In contrast to the LDT NCA insert the LDT DCA insert appears similar to the unused DCA insert with only a slight dark discoloration at the upstream end. The phases observed include primarily cubic W with cubic Ba_2CaWO_6 (space group:Fm-3m (Ref. 59)). The cubic Ba_2CaWO_6 phase is the only known ternary compound in the CaO-BaO- WO_3 system and is found to be stable at 1200 °C (Ref. 52). The Ba_2CaWO_6 phase has been identified on previous lifetime tested NASA cathode inserts (Ref. 58). The XRD scans at the central and upstream sections indicate that the quantity of the Ba_2CaWO_6 phase increases along the axial length with the highest content near the upstream end. The discoloration observed on the inner surface of the insert matches the trend.

4.5 Emission Surface Topographical Morphology

The inner emission surfaces were evaluated with SEM using both SE and BSE detectors to highlight topography and chemical composition, respectively. Only the SE micrographs are presented below for brevity, the BSE micrographs are useful for identification of phases but do not provide significant additional information on the topography. Summary of the BSE micrographs are discussed in text along with the SE micrographs shown below. The four inserts were evaluated at the downstream, central, and upstream axial locations. The inserts were examined with a 45° inclination angle to emphasize topography. The SE images of the NCA inserts are shown in Figure 8, with unused insert to the left and the corresponding micrograph of the LDT insert to the right. Figure 9 shows the same regions and magnifications for the DCA inserts, again with unused insert on the left and LDT on the right. EDS scans across the full field of view reveal that the unused inserts contain only the tungsten matrix, with no impregnate or tungstate phases. The microstructure of the unused inserts was fairly invariant with axial location. The tungsten matrix is composed primarily of smooth grains with open porosity on the order of the impregnate grains observed in the cross-sections. For an unknown reason the downstream portion of the unused NCA insert, Figure 8(a), has a rough almost fractured looking tungsten matrix. Possibly this is an artifact of handling or sample preparation, the issue was not further investigated.

The LDT NCA insert has a comparable microstructure to the unused NCA insert. The LDT NCA insert is composed of primarily a tungsten matrix with open porosity and decorations of other phases as confirmed with EDS. The quantity and geometric dimensions of the pores is similar between the unused and LDT inserts. The morphology of the alternative phases vary with axial location. The downstream region of the LDT NCA insert, Figure 8(b), has a slightly faceted nature of the tungsten matrix possibly indicating an etching or erosion mechanism. Likely as tungsten is consumed to form the alternative phases, the resulting influence on the matrix is a faceted appearance. The $\text{BaCa}(\text{CO}_3)_2$ phase appears as a sub-micron fine grained deposition. The thickness and quantity of the deposition varies with location from sparse as shown in Figure 8(b), to agglomerated regions covering 50 to 100 μm . Open porosity and tungsten matrix can be identified in both sparse and agglomerated regions. The central region of the LDT NCA insert, Figure 8(d), has a less faceted tungsten matrix with nearly unaltered morphology from the unused insert. Deposition of the $\text{Ba}_4\text{Al}_2\text{O}_7$, Ba_3WO_6 , $\text{Ba}_3\text{Al}_2\text{O}_6$ phases appears as smooth grains with comparable size to the tungsten grains. The similarity between the tungsten grains and alternative phases makes identification difficult in SE micrographs, but BSE micrographs combined with EDS scans help to

reveal the phases. The upstream region of the LDT NCA insert, Figure 8(f), has the largest deviation from the unused insert. The tungsten matrix appears somewhat faceted and contains a high density of cracks. Open porosity exists but is limited compared to the unused insert and the remainder of the LDT NCA insert. The $\text{Ba}_3\text{W}_2\text{O}_9$, Ba_2WO_5 , Ba_3WO_6 , and BaWO_4 phases appear as a cracked set of grains partially filling the voids.

The LDT DCA insert in general has a more severe faceting of the tungsten matrix than the LDT NCA insert. The downstream and central regions of the LDT DCA insert, Figure 9(b) and (d), have a particularly faceted appearance with smooth faces as large as $20\text{ }\mu\text{m}$. EDS scans across the full field of view reveal the surface to be composed of only tungsten. The upstream region of the LDT DCA insert, Figure 9(f), has a slightly faceted tungsten matrix with a sub-micron fine grain deposition of Ba_2CaWO_6 . Open pore porosity comparable to the unused DCA insert is found throughout the insert.

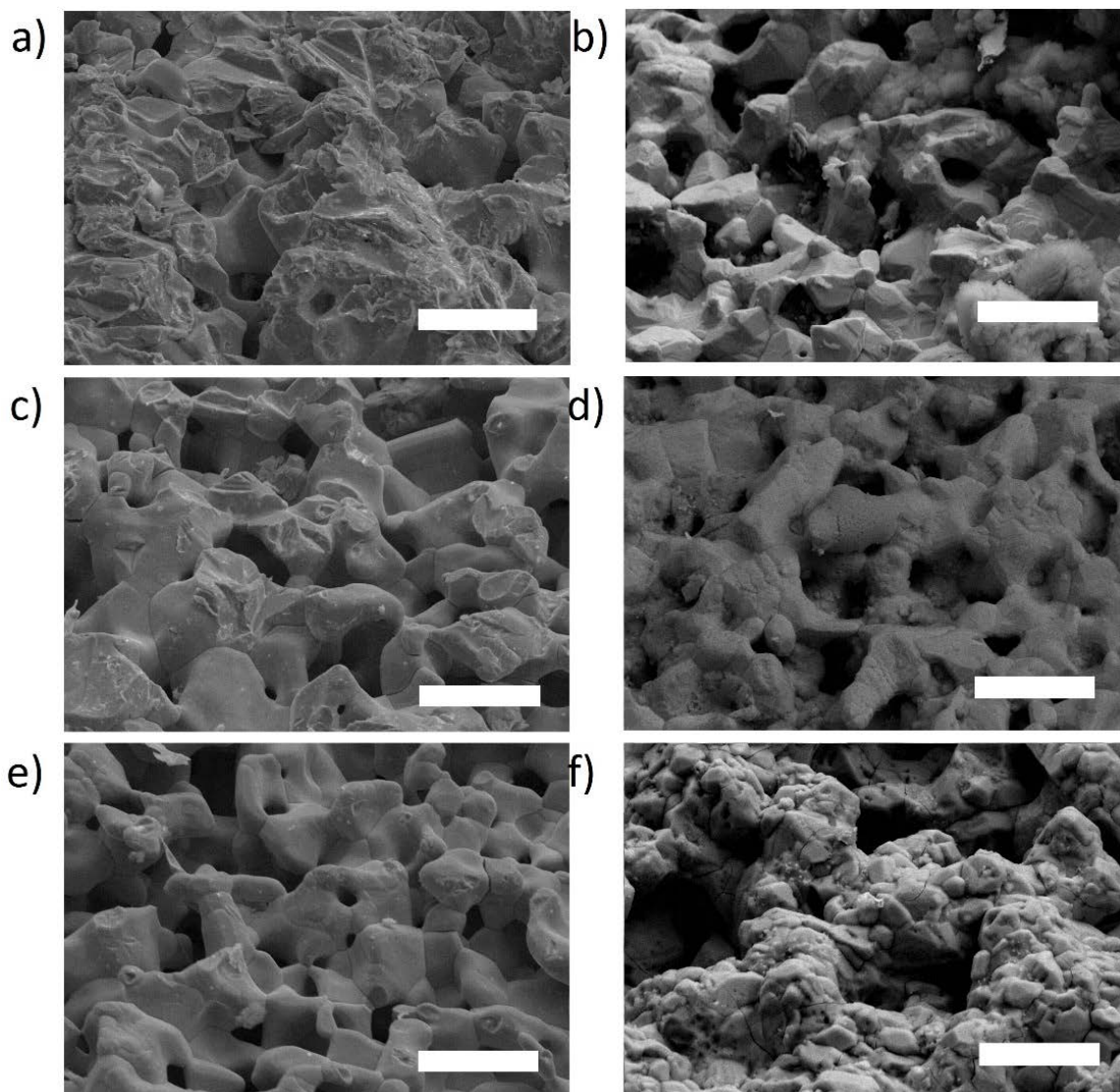


Figure 8.—NCA insert SE micrographs, all scale bars are $10\text{ }\mu\text{m}$. (a) Unused NCA downstream, (b) LDT NCA downstream, (c) unused NCA central, (d) LDT NCA central, (e) unused NCA upstream, (f) LDT NCA upstream.

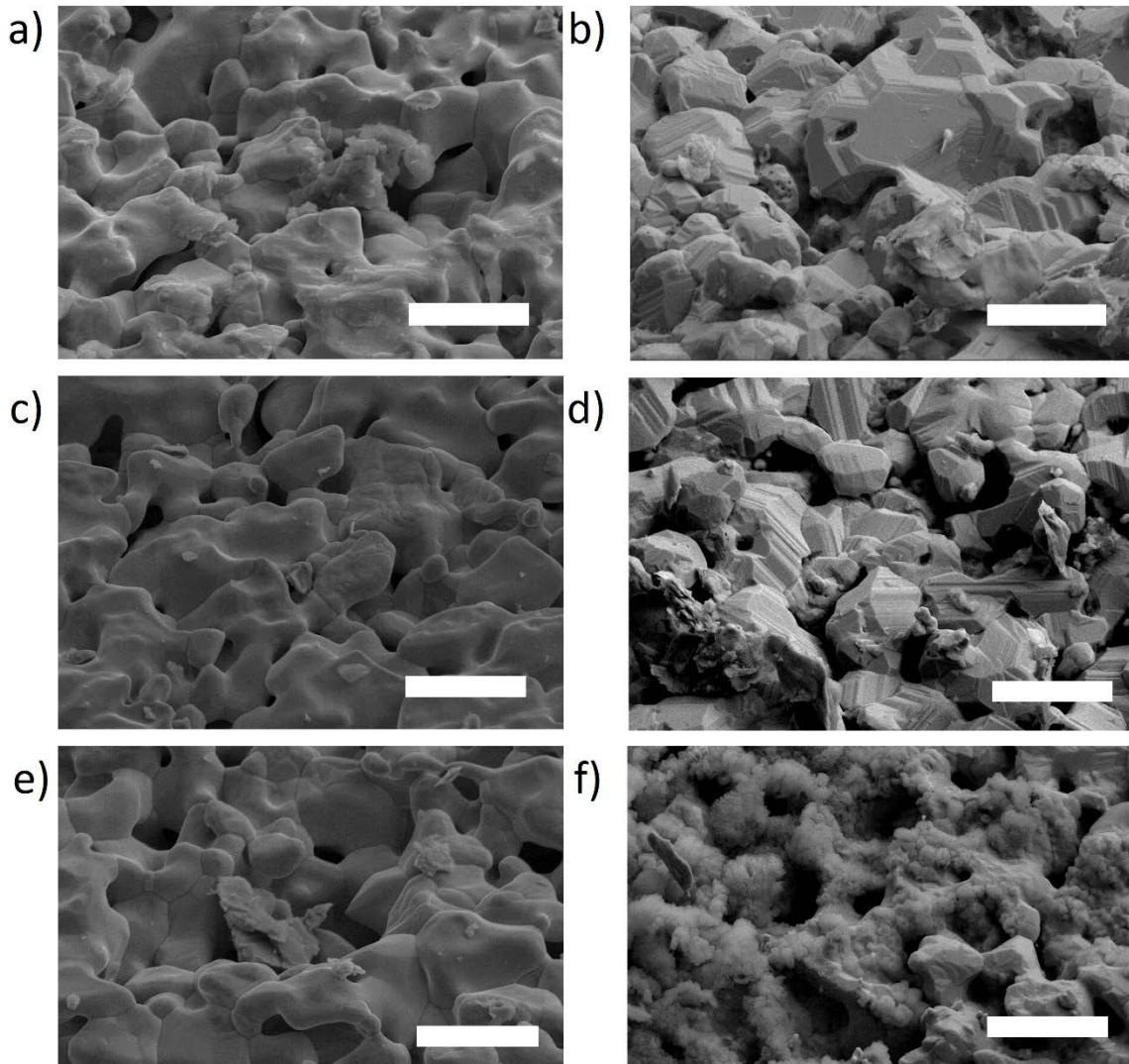


Figure 9.—DCA insert SE micrographs, all scale bars are 10 μm . (a) Unused DCA downstream, (b) LDT DCA downstream, (c) unused DCA central, (d) LDT DCA central, (e) unused DCA upstream, (f) LDT DCA upstream.

5.0 Conclusion

The NEXT long-duration test cathode inserts have been destructively analyzed and evaluated in an effort to better understand cathode behavior during long operating periods. The post-test cathode inserts have been compared whenever possible to unused inserts of similar quality and fidelity. It has been determined that the impregnate grain size, distribution, and area fraction were not altered significantly during the long-duration test. In general, the etch regions of the inserts were found to decrease during the test by 20 to 30 percent, with the exception of the outer etch region near the upstream axial location which increased in size. Barium distributions in the inserts were investigated in an attempt to quantify barium loss. A barium depletion zone was identified in the downstream axial region of the post-test DCA insert, with depletion depths between 45 to 88 μm of the emission surface. No similar barium depletion zone was identified in the post-test NCA insert or either of the unused inserts. A bulk difference in $\text{BaO}/\text{Al}_2\text{O}_3$ content was measured between the post-test and unused inserts. The magnitude of the difference was within experimental uncertainty for the NCA insert, but the DCA insert exhibited 30 percent lower $\text{BaO}/\text{Al}_2\text{O}_3$ content in the post-test insert than the unused insert. Visual bands of varying contrast were observed on the inner surface of the post-test inserts, x-ray diffraction was used to determine phase.

A number of phases were found present on the inner surfaces of the inserts. The DCA insert only contained one barium-calcium-tungstate phase while the NCA insert contained several barium-tungstate phases, barium-aluminate phases, and a barium-calcium-carbonate phase. The inner surfaces of the inserts were found to contain a tungsten matrix with an open network of pores in both the unused and post-test inserts. No significant buildup of tungstate phases was observed.

References

1. Brophy, J.R., et al., "Development and Testing of the Dawn Ion Propulsion System," *42nd AIAA/ASME/SAE/ASEE Joint Propulsion Conference and Exhibit*, AIAA-2006-4319, Sacramento, CA, July 9–12, 2006.
2. Patterson, M.J. and Benson, S.W., "NEXT Ion Propulsion System Development Status and Performance," *43rd AIAA/ASME/SAE/ASEE Joint Propulsion Conference and Exhibit*, AIAA-2007-5199, Cincinnati, OH, July 8–11, 2007.
3. Polk, J.E., et al., "Demonstration of the NSTAR Ion Propulsion System on the Deep Space One Mission," *27th International Electric Propulsion Conference*, IEPC-2001-075, Pasadena, CA, October 15–19, 2001.
4. Rayman, M.D., "The Successful Conclusion of the Deep Space 1 Mission: Important Results Without a Flashy Title," *Space Technology*, Vol. 23, No. 2-3, 2003, pp. 185–196.
5. Benson, S.W. and Patterson, M.J., "NASA's Evolutionary Xenon Thruster (NEXT) Ion Propulsion Technology Development Status in 2009," *31st International Electric Propulsion Conference*, IEPC-2009-150, Ann Arbor, MI, September 20–24, 2009.
6. Hoskins, W.A., Aadland, R.S., Meckel, N.J., Talerico, L.A., and Monheiser, J.M., "NEXT Ion Propulsion System Production Readiness," *43rd AIAA/ASME/SAE/ASEE Joint Propulsion Conference and Exhibit*, AIAA-2007-5856, Cincinnati, OH, July 8–11, 2007.
7. Patterson, M.J., et al., "NEXT Multi-Thruster Array Test - Engineering Demonstration," *42nd AIAA/ASME/SAE/ASEE Joint Propulsion Conference and Exhibit*, AIAA-2006-5180, Sacramento, CA, July 9–12, 2006.
8. Snyder, J.S., Anderson, J.R., Van Noord, J.L., and Soulas, G.C., "Environmental Testing of the NEXT PM1 Ion Engine," *43rd AIAA/ASME/SAE/ASEE Joint Propulsion Conference and Exhibit*, AIAA-2007-5275, Cincinnati, OH, July 8–11, 2007.
9. Soulas, G.C., Patterson, M.J., Pinero, L., Herman, D.A., and Snyder, J.S., "NEXT Single String Integration Test Results," *45th AIAA/ASME/SAE/ASEE Joint Propulsion Conference and Exhibit*, AIAA-2009-4816, Denver, CO, August 2–5, 2009.
10. Aadland, R.S., Frederick, H., Benson, S.W., and Malone, S.P., "Development Results of the NEXT Propellant Management System," *JANNAF 2nd Liquid Propulsion Subcommittee and 1st Spacecraft Propulsion Subcommittee Joint Meeting*, JANNAF 2005-0356DW, Monterey, CA, December 5–8, 2005.
11. Crofton, M.W., et al., "Characterization of the NASA NEXT Thruster," *45th AIAA/ASME/SAE/ASEE Joint Propulsion Conference and Exhibit*, AIAA-2009-4815, Denver, CO, August 2–5, 2009.
12. Diamant, K.D., Pollard, J.E., Crofton, M.W., Patterson, M.J., and Soulas, G.C., "Thrust Stand Characterization of the NASA NEXT Thruster," *46th AIAA/ASME/SAE/ASEE Joint Propulsion Conference & Exhibit*, AIAA-2010-6701, Nashville, TN, July 25–28, 2010.
13. Herman, D.A., Pinero, L.R., and Sovey, J.S., "NASA's Evolutionary Xenon Thruster (NEXT) Component Verification Testing," *44th AIAA/ASME/SAE/ASEE Joint Propulsion Conference and Exhibit*, AIAA-2008-4812, Hartford, CT, July 21–23, 2008.
14. Herman, D.A., Soulas, G.C., and Patterson, M.J., "Performance Evaluation of the Prototype-Model NEXT Ion Thruster," *43rd AIAA/ASME/SAE/ASEE Joint Propulsion Conference and Exhibit*, AIAA-2007-5212, Cincinnati, OH, July 8–11, 2007.

15. Pinero, L.R., Hopson, M., Todd, P.C., and Wong, B., "Performance of the NEXT Engineering Model Power Processing Unit," *43rd AIAA/ASME/SAE/ASEE Joint Propulsion Conference and Exhibit*, AIAA-2007-5214, Cincinnati, OH, July 8–11, 2007.
16. Pollard, J.E., Diamant, K.D., Crofton, M.W., Patterson, M.J., and Soulas, G.C., "Spatially-Resolved Beam Current and Charge-State Distributions for the NEXT Ion Engine," *46th AIAA/ASME/SAE/ASEE Joint Propulsion Conference and Exhibit*, AIAA-2010-6779, Nashville, TN, July 25–28, 2010.
17. Snyder, J.S., et al., "Vibration Test of a Breadboard Gimbal for the NEXT Ion Engine," *42nd AIAA/ASME/SAE/ASEE Joint Propulsion Conference and Exhibit*, AIAA-2006-4665, Sacramento, CA, July 9–12, 2006.
18. Van Noord, J.L., "Lifetime Assessment of the NEXT Ion Thruster," *43rd AIAA/ASME/SAE/ASEE Joint Propulsion Conference and Exhibit*, AIAA-2007-5274, Cincinnati, OH, July 8–11, 2007.
19. Van Noord, J.L. and Herman, D.A., "Application of the NEXT Ion Thruster Lifetime Assessment to Thruster Throttling," *44th AIAA/ASME/SAE/ASEE Joint Propulsion Conference and Exhibit*, AIAA-2008-4526, Hartford, CT, July 21–23, 2008.
20. Soulas, G.C., Kamhawi, H., Patterson, M.J., Britton, M.A., and Frandina, M.M., "NEXT Ion Engine 2000 Hour Wear Test Results," *40th AIAA/ASME/SAE/ASEE Joint Propulsion Conference and Exhibit*, AIAA-2004-3791, Fort Lauderdale, FL, July 11–14, 2004.
21. Van Noord, J.L., Soulas, G.C., and Sovey, J.S., "NEXT PM1R Ion Thruster and Propellant Management System Wear Test Results," *31st International Electric Propulsion Conference*, IEPC-2009-163, Ann Arbor, MI, September 20–24, 2009.
22. Shastry, R., Herman, D.A., Soulas, G.C., and Patterson, M.J., "End-of-test Performance and Wear Characterization of NASA's Evolutionary Xenon Thruster (NEXT) Long-Duration Test," *50th AIAA/ASME/SAE/ASEE Joint Propulsion Conference*, AIAA-2014-3617, Cleveland, OH, July 28–30, 2014.
23. Shastry, R. and Soulas, G.C., "Post-test Inspection of NASA's Evolutionary Xenon Thruster Long-Duration Test Hardware: Discharge and Neutralizer Cathodes," *52nd AIAA/SAE/ASEE Joint Propulsion Conference*, Salt Lake City, UT, July 25–27, 2016.
24. Soulas, G.C. and Shastry, R., "Post-test Inspection of NASA's Evolutionary Xenon Thruster Long Duration Test Hardware: Ion Optics," *52nd AIAA/SAE/ASEE Joint Propulsion Conference*, Salt Lake City, UT, July 25–27, 2016.
25. Shastry, R. and Soulas, G.C., "Post-test Inspection of NASA's Evolutionary Xenon Thruster Long-Duration Test Hardware: Discharge Chamber," *52nd AIAA/SAE/ASEE Joint Propulsion Conference*, Salt Lake City, UT, July 25–27, 2016.
26. Hoskins, W.A., et al., "Development of a Prototype Model Ion Thruster for the NEXT System," *40th AIAA/ASME/SAE/ASEE Joint Propulsion Conference and Exhibit*, AIAA-2004-4111, Fort Lauderdale, FL, July 11–14, 2004.
27. Soulas, G.C. and Patterson, M.J., "NEXT Ion Thruster Performance Dispersion Analyses," *43rd AIAA/ASME/SAE/ASEE Joint Propulsion Conference and Exhibit*, AIAA-2007-5213, Cincinnati, OH, July 8–11, 2007.
28. Frandina, M.M., Arrington, L.A., Soulas, G.C., Hickman, T.A., and Patterson, M.J., "Status of the NEXT Ion Thruster Long Duration Test," *41st AIAA/ASME/SAE/ASEE Joint Propulsion Conference and Exhibit*, AIAA-2005-4065, Tucson, AZ, July 10–13, 2005.
29. Herman, D.A., Soulas, G.C., and Patterson, M.J., "Performance Characteristics of the NEXT Long-Duration Test after 16,550 h and 337 kg of Xenon Processed," *44th AIAA/ASME/SAE/ASEE Joint Propulsion Conference and Exhibit*, AIAA-2008-4527, Hartford, CT, July 21–23, 2008.
30. Herman, D.A., Soulas, G.C., and Patterson, M.J., "NEXT Long-Duration Test Plume and Wear Characteristics after 16,550 h of Operation and 337 kg of Xenon Processed," *44th AIAA/ASME/SAE/ASEE Joint Propulsion Conference and Exhibit*, AIAA-2008-4919, Hartford, CT, July 21–23, 2008.

31. Patterson, M.J., et al., "NEXT: NASA's Evolutionary Xenon Thruster," *38th AIAA/ASME/SAE/ASEE Joint Propulsion Conference and Exhibit*, AIAA-2002-3832, Indianapolis, IN, July 7–10, 2002.
32. Soulas, G.C., Domanikos, M.T., and Patterson, M.J., "Performance Evaluation of the NEXT Ion Engine," *39th AIAA/ASME/SAE/ASEE Joint Propulsion Conference and Exhibit*, AIAA-2003-5278, Huntsville, AL, July 20–23, 2003.
33. Herman, D.A., Soulas, G.C., and Patterson, M.J., "Status of the NEXT Long-Duration Test after 23,300 Hours of Operation," *45th AIAA/ASME/SAE/ASEE Joint Propulsion Conference and Exhibit*, AIAA-2009-4917, Denver, CO, August 2–5, 2009.
34. Herman, D.A., "Status of the NASA's Evolutionary Xenon Thruster (NEXT) Long-Duration Test after 30,352 Hours of Operation," *46th AIAA/ASME/SAE/ASEE Joint Propulsion Conference and Exhibit*, AIAA-2010-7112, Nashville, TN, July 25–28, 2010.
35. Herman, D.A., "NASA's Evolutionary Xenon Thruster (NEXT) Project Qualification Propellant Throughput Milestone: Performance, Erosion, and Thruster Service Life Prediction after 450 kg," *JANNAF 7th Modeling and Simulation, 5th Liquid Propulsion, and 4th Spacecraft Propulsion Joint Subcommittee Meeting*, CPIAC JSC 2010-0015EH and NASA/TM—2010-216816, Colorado Springs, CO, May 3–7, 2010.
36. Herman, D.A., "Review of the NASA's Evolutionary Xenon Thruster (NEXT) Long-Duration Test as of 632 kg of Propellant Throughput," *47th AIAA/ASME/SAE/ASEE Joint Propulsion Conference and Exhibit*, AIAA-2011-5658, San Diego, CA, July 31–August 3, 2011.
37. Herman, D.A., Soulas, G.C., and Patterson, M.J., "Status of the NEXT Ion Thruster Long-Duration Test after 10,100 h and 207 kg Demonstrated," *43rd AIAA/ASME/SAE/ASEE Joint Propulsion Conference and Exhibit*, AIAA-2007-5272, Cincinnati, OH, July 8–11, 2007.
38. Herman, D.A., Soulas, G.C., and Patterson, M.J., "NEXT Long-Duration Test Neutralizer Performance and Erosion Characteristics," *31st International Electric Propulsion Conference*, IEPC-2009-154, Ann Arbor, MI, September 20–24, 2009.
39. Herman, D.A., Soulas, G.C., Van Noord, J.L., and Patterson, M.J., "NASA's Evolutionary Xenon Thruster Long-Duration Test Results," *Journal of Propulsion and Power*, Vol. 28, No. 3, May - June, 2012, pp. 625–635.
40. Shastry, R., Herman, D.A., Soulas, G.C., and Patterson, M.J., "NASA's Evolutionary Xenon Thruster (NEXT) Long-Duration Test as of 736 kg of Propellant Throughput," *48th AIAA/ASME/SAE/ASEE Joint Propulsion Conference and Exhibit*, AIAA-2012-4023, Atlanta, GA, July 29–August 1, 2012.
41. Shastry, R., Herman, D.A., Soulas, G.C., and Patterson, M.J., "Status of NASA's Evolutionary Xenon Thruster (NEXT) Long-Duration Test as of 50,000 h and 900 kg Throughput," *33rd International Electric Propulsion Conference*, IEPC-2013-121, Washington D.C., October 6–10, 2013.
42. Sengupta, A., et al., "The 30,000-Hour Extended-Life Test of the Deep Space 1 Flight Spare Ion Thruster," NASA/TP—2004-213391, March, 2005.
43. Kan, H.K.A. and Seaver, R.R., "Impregnate Composition in Dispenser Cathodes," SD-TR-85-50, August, 1985.
44. Polk, J.E., Capece, A.M., Mikellides, I.G., and Katz, I., "Barium Depletion in the NSTAR Discharge Cathode After 30,472 Hours of Operation," *46th AIAA/ASME/SAE/ASEE Joint Propulsion Conference and Exhibit*, AIAA-2010-6702, Nashville, TN, July, 2010.
45. Polk, J.E., Mikellides, I.G., Capece, A.M., and Katz, I., "Barium Depletion in Hollow Cathode Emitters," *J. Appl. Phys.* 119, 023303, 2016.
46. PDF 04-007-8737, ICDD, 2010.
47. PDF 00-0027-0032, ICDD, 2010.
48. PDF 00-041-0165, ICDD, 1989.
49. PDF 04-007-8522, ICDD, 2010.
50. PDF 04-009-7460, ICDD, 2010.

51. Wolten, G.M., "An appraisal of the ternary system BaO-CaO-Al₂O₃," SD-TR-80-67, TR-0080(5911)-1, 1980.
52. Kreidler, E.R., "Phase Equilibria in the System CaO-BaO-WO₃," J. Amer. Ceram. Soc., Vol. 55 No. 10, 1972.
53. Rittner, E., Rutledge, W., and Ahlert, R., "On the Mechanism of Operation of the Barium Aluminate Impregnated Cathode," J. Appl. Phys. Vol. 28 No. 12, 1957.
54. PDF 04-010-8664, ICDD, 2010.
55. PDF 04-014-6836, ICDD, 2010.
56. PDF 04-002-0803, ICDD, 2010.
57. Schoenbeck, L., "Investigation of Reactions Between Barium Compounds and Tungsten in a Simulated Reservoir Hollow Cathode Environment," Masters Thesis, Georgia Institute of Technology, February, 2005.
58. Sarver-Verhey, T., "Destructive Evaluation of a Xenon Hollow Cathode After a 28,000 Hour Life Test," 34th AIAA/ASME/SAE/ASEE Joint Propulsion Conference, AIAA 98-3482, 1998.
59. PDF 04-015-6802, ICDD, 2011.

